The Response of Tropical Rainfall to Idealized Small-Scale Thermal and Mechanical Forcing

Martin Velez-Pardo[1], **Timothy W. Cronin**[1]

[1]Program in Atmospheres, Oceans and Climate, Massachusetts Institute of Technology, Cambridge, MA 02139

Key Points:

- Convective rainfall triggered by different thermodynamic and mechanical forcings can exhibit markedly different Gross Moist Stabilities.
- Mechanically-induced, low-level convergence is an effective mechanism of net precipitation enhancement.
- All forcing types collapse onto the same curve relating column relative humidity and rainfall.

Corresponding author: Martin Velez-Pardo, `martinvp@mit.edu`

Abstract

[Predicting the spatiotemporal distribution of rainfall remains a key challenge in Tropical Meteorology, partly due to an incomplete understanding of the effects of different environmental factors on atmospheric convection. In this work, we use numerical simulations of tropical ocean domains to study how rainfall responds to imposed localized thermal and mechanical forcings to the atmosphere. We use the Normalized Gross Moist Stability—NGMS—to quantify the net precipitation response associated with a given net atmospheric heating. We find that NGMS values differ considerably for different forcings, but show that the relationship between precipitation and column relative humidity collapses along a universal curve across all of them. We also show that the vertical component of the Gross Moist Stability only approximates the NGMS well at scales larger than a couple hundred kilometers, indicating that general horizontal mixing processes are not negligible at smaller scales.]

Plain Language Summary

[Predicting where rain tends to occur in tropical areas is challenging. In this work, we simulate a small area of atmosphere over a tropical ocean to study how rainfall changes when we alter the surface temperature, the atmospheric heating rate at different heights, and the pressure gradients that drive the winds near the surface. We find that such alterations lead to self-consistent but different relationships between the amount of rainfall produced and the net heating of the atmosphere. We show that the spatial extent of the alteration affects how well this relationship can be inferred from horizontally-averaged atmospheric properties. In contrast, we find that the relationship between rainfall and the average relative humidity in the atmosphere remains the same across all types of environmental alterations.]

1 Introduction

What makes it rain where it does in the tropics? Two distinct, influential paradigms often invoked to answer this question are those proposed by Lindzen and Nigam (1987), and by Neelin and Held (1987). Lindzen and Nigam argued that maxima in precipitation are controlled by low-level wind convergence that is mechanically forced by boundary-layer pressure gradients associated with sea-surface temperature—SST—patterns. On the other hand, Neelin and Held posited that maxima of deep convection and rainfall are regulated by a combination of the net column energy input, and the "Gross Moist Stability" (GMS) – a metric of how efficiently ascending circulations export this energy surplus. These are representative of what we refer to subsequently as "mechanical" and "column-energetic" schools of thought. These schools are united in the importance they assign to determining patterns of vertical motion, which regulate atmospheric moisture import and thus the amount by which local precipitation exceeds local evaporation. In this work, we use idealized simulations to examine the impacts of both mechanical and column-energetic (or thermodynamic) forcings on precipitation. We focus on scales ranging from tens to a few hundred kilometers, given their significant relevance for human communities and ecosystems, and the size constraints of simulations at cloud- and cloud-system-resolving scales.

The success of column-energetic arguments in accounting for large-scale precipitation patterns and zonal-mean shifts is well-documented (Donohoe et al., 2013; Marshall et al., 2014; Bischoff & Schneider, 2014; Schneider et al., 2014; Boos & Korty, 2016). However, establishing the value of the GMS in advance poses a singular challenge for predictive uses of the column-energetic approach. Additionally, its explanatory power fails for phenomena at finer scales, for instance the behavior of the narrow East-Pacific Intertropical Convergence Zone (ITCZ) (Sobel & Neelin, 2006; Back & Bretherton, 2006), or precipitation over small islands in idealized models (Cronin et al., 2015). Furthermore,

the column-energetic view does little to explain rainfall maxima over orography, which provide critical water supplies for billions of people. In these contexts, the contribution of mechanically induced convergence, ignored by column energetics, seems to play a pivotal role.

Several modeling studies have explored the sensitivity of deep convection and rainfall to forcings of different kinds. Derbyshire et al. (2004) used a CRM with adjusted drying at different heights, allowing the model to relax to a prescribed profile of relative humidity, and found that a strong drying in the mid-troposphere suppressed deep convection and led to shallow convection. Using a CRM under the Weak Temperature Gradient approximation (WTG), Wang and Sobel (2012) found that mid- and lower-tropospheric drying led to lower precipitation than upper-tropospheric drying. In turn, Anber et al. (2015) separately prescribed heating throughout the depth of the atmospheric column, and surface enthalpy flux anomalies, and showed that, while the former led to more precipitation for forcings close to the RCE reference, total precipitation responded more sensitively to changes in surface enthalpy fluxes than to atmospheric heating, per change in $\mathrm{W/m^2}$ of forcing.

In this letter, we study how different thermodynamic and mechanical mechanisms affect time-mean rainfall at scales of tens to a few hundred kilometers. We run numerical simulations of convection over idealized ocean domains in a CRM, where we introduce three types of forcings, illustrated in Figure 1:

- Localized SST anomalies,
- vertically and horizontally localized heating at different heights,
- mechanical forcing of the horizontal winds consistent with localized convergence.

We use these forcings as an idealized way of separately probing how phenomena such as aerosol-induced warming at different levels, narrow regions of high SST, or wind convergence induced by orography or large-scale circulations, affect tropical rainfall patterns. We characterize the effects of the forcings, and discuss the implications of analyzing their behavior in terms of two metrics of the Gross Moist Stability, and the relationship between precipitation and column moisture. We also assess how the spatial scale of the forcings affects both rainfall and the properties of the ascending circulations over the forced patch.

2 Methods

We perform numerical simulations in radiative-convective equilibrium using the System for Atmospheric Modeling, SAM (Khairoutdinov & Randall, 2003), version 6.10.6. The basic setup consists of a domain over an ocean surface that is doubly-periodic in the horizontal, with 1024 by 32 grids in the horizontal at 3 km spacing, and a stretched grid with 64 vertical levels. We use the same parameterization schemes as Cronin et al. (2015), and initialize our runs from profiles of temperature and humidity in radiative-convective equilibrium (RCE) with an all-ocean surface.

For all simulations performed, perturbations are prescribed over or along the edges of a reference patch region that spans the whole short dimension of the channel, and has half-width of 24 km in the long dimension (unless indicated otherwise). The surface is allowed to evaporate freely, and its temperature is fixed at 300.2 K, except for the SSTA simulations described below. We follow Cronin (2014) in prescribing a solar latitude of 45° and a solar constant of 560 $\mathrm{Wm^{-2}}$ and a zenith angle of 56.26°, which yield an insolation of 311 $\mathrm{Wm^{-2}}$. To prevent convective aggregation, all of our runs homogenize radiation across the domain. We perform three main groups of forced simulations (Figure 1). All of our simulations are run for 75 days, with the last 50 days used for the analysis.

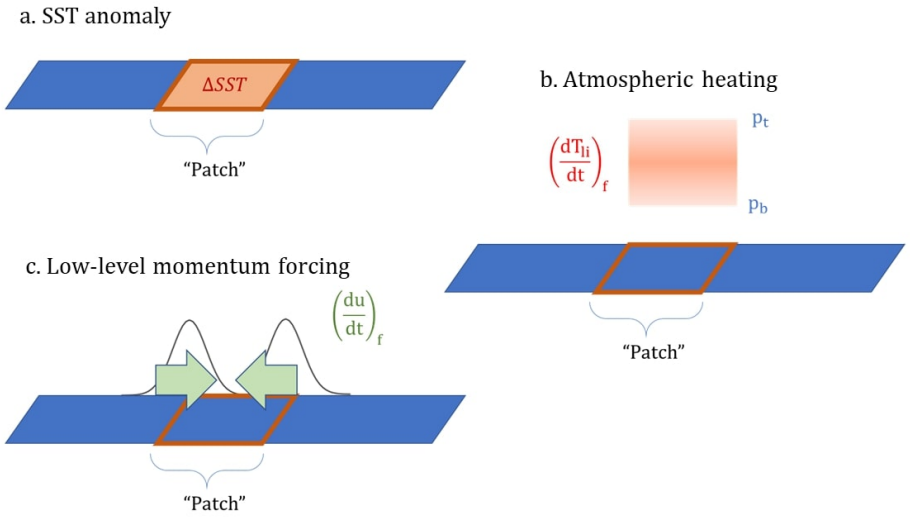

Figure 1. Sketches of the setups representing the three different forcings: a. Sea-surface temperature anomaly, b. Atmospheric heating between levels p_b and p_t , c. Low-level momentum forcing. The reference patch for which averages are calculated is indicated in red; geometry is not to scale.

2.0.1 Numerical Experiment 1: SST anomalies

For the first set of simulations, denoted by SSTA, we prescribe a constant surface temperature anomaly for the area of the patch given by $SST(x, y) = T_0 + \Delta T$ if (x, y) are contained within the patch, and T_0 otherwise, where $T_0 = 300.2$ K is the reference surface temperature. We run simulations with ΔT taking values of $-0.4, -0.1, 0.1, 0.4, 0.7, 1.0, 1.5$ and 2.0 K.

2.0.2 Numerical Experiment 2: Localized atmospheric heating at different levels

To assess the convective response to heating at different levels, we add a forcing term Q to the equation for the liquid water/ice static energy h_{li}:

$$\frac{dh_{li}}{dt}(p, t) = (...) + Q \tag{1}$$

For the forcing, we choose a half-sinusoidal shape in the vertical, constrained between two pressure levels, uniform values in the horizontal within the patch region, and zero outside.

$$Q = M \sin\left(\pi \frac{p - p_t}{p_b - p_t}\right) \tag{2}$$

where M is the maximum amplitude of the forcing, p is the pressure, and p_t and p_b are the pressure levels at the top and at the bottom of the heated layer, respectively. This yields an expression for M in terms of the integrated column forcing, Q_f, namely

$$M = \frac{g\pi Q_f}{2c_p(p_b - p_t)}, \tag{3}$$

obtained from the mass-weighted integral of $c_p Q$ in the vertical. For instance, $Q_f = 1$ W/m^2 corresponds to $M = 2.05{\cdot}10^{-7}$K/s. We perform simulations with values of Q_f of $-10, -5, 5, 10, 20, 40$ and 50 W/m^2, and apply the thermal forcings at four different levels:

- Qlb: $p_b = 1000$ hPa, $p_t = 900$ hPa,
- Qlt: $p_b = 900$ hPa, $p_t = 800$ hPa,
- Qm: $p_b = 700$ hPa, $p_t = 400$ hPa,
- Qu: $p_b = 500$ hPa, $p_t = 200$ hPa,

which represent the boundary layer, the lower free troposphere, and mid- and upper-tropospheric layers, respectively.

2.0.3 Numerical Experiment 3: Low-level wind forcing

The last set of numerical simulations examines the effects of purely mechanical low-level convergence on rainfall over the patch region without forced thermal gradients in the boundary layer. To do this, we introduce a forcing F_m in the along-channel component (x) of the momentum equation, namely

$$\frac{du}{dt} = (...) + F_m \tag{4}$$

For simplicity, we assume a Gaussian-shaped distribution for the forcing, centered at each border of the strip (x_0), with standard deviation σ_m of 12 km, and a vertical decay scale h_l of 500 m. That is,

$$F_m(x,z) = \beta \exp\left(-\frac{(x-x_0)^2}{2\sigma_m^2}\right) \exp\left(\frac{-z}{h_l}\right) \tag{5}$$

Where β is the maximum imposed acceleration. F_m can be interpreted as an additional pressure gradient force, and its integral, through Bernoulli's principle, can be interpreted as a maximum consequent inflow speed in the absence of friction.

$$\int_{-\infty}^{\infty} F_m dx = \frac{\Delta P}{\rho} = \frac{u_{max}^2}{2} \tag{6}$$

This relationship allows us to relate the forcing strength β to a maximal convergent wind speed u_{max}:

$$\beta = \frac{u_{max}^2}{2\sigma_m\sqrt{2\pi}} \tag{7}$$

We perform momentum forcing simulations using values of u_{max} set at $-2, -1, 1, 2, 3, 5, 7$ and 10 m/s, where the negative values signify an imposed tendency for winds to blow out of the patch. We note that, while β and u_{max} do not depend on h_l, h_l is expected to affect the strength of rainfall by modulating the depth of the convergent flow.

3 Results

3.1 Different convective responses to different forcings

All surface and low-level forcings, namely SSTA, Qlb, Qlt and MF, result in a significant response in $P-E$, the precipitation minus evaporation or "net precipitation", over the reference patch, as shown in Figure 2. In contrast, imposed mid- and upper-level heating produces negligible changes in $P-E$. This finding agrees with Wang and Sobel (2012), who showed a weaker sensitivity of precipitation responses to drying anomalies in the upper troposphere in WTG simulations over oceans.

Our simulations also show that low-level forcings produce different responses in $P-E$ over the patch, as indicated by the slopes of the lines in figure 2a. Following Raymond et al. (2009), we define the Normalized Gross Moist Stability—NGMS henceforth—as the quantity mediating the relationship between the atmospheric heating rate or entropy forcing, $\dot{Q}_{atm}$, and net precipitation $P-E$. The entropy forcing is calculated as $\dot{Q}_{atm} = LHF + SHF + \dot{Q}_{rad} + Q_f$, where LHF and SHF are the surface latent and sensible

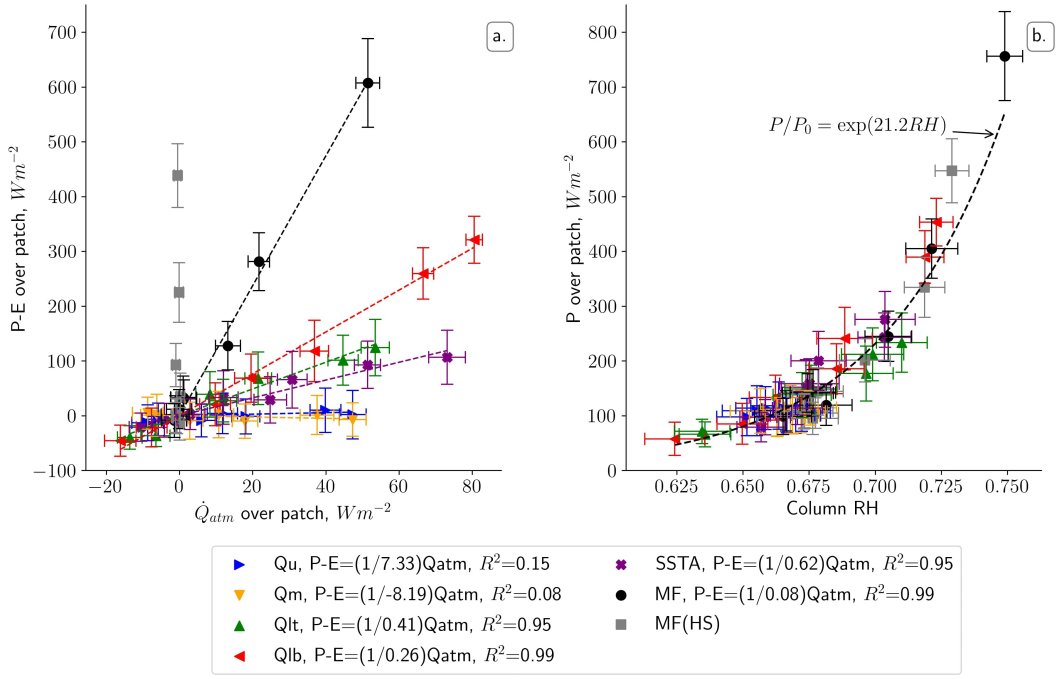

Figure 2. (a) $P - E$ vs. $\dot{Q}_{atm}$ over reference patch for simulations forced with atmospheric heating (triangles), SST anomaly (purple exes), low-level momentum (black circles), and low-level momentum with homogenized surface fluxes (gray squares; MF(HS)). For Qlb, Qlt, SSTA and MF, a linear fit is shown whose slope corresponds to the NGMS. Error bars indicate ±2 standard errors of the mean of daily values. (b) Precipitation vs. mean atmospheric column relative humidity—CRH–over reference patch. Dashed line shows exponential fit.

heat fluxes, respectively, $\dot{Q}_{rad}$ is the radiative heating rate, and Q_f is the imposed heating. Denoting the NGMS by Γ_R, we write

$$P - E = \frac{1}{\Gamma_R}\dot{Q}_{atm}. \tag{8}$$

A higher value of NGMS indicates thus a less efficient conversion of the net heating into net precipitation.

A central result of this work is that the net precipitation response to distinct types of low-level forcing results in distinct values of NGMS. A forcing-dependent NGMS is reasonably well-defined for each type of low-level forcing because $P-E$ varies linearly with $\dot{Q}_{atm}$. The linearity of convective responses to transient as well as steady perturbations to the SST and the atmospheric water vapor has been shown in previous simulation based on the Weak Temperature Gradient approximation (Kuang, 2012; Wang & Sobel, 2012; Anber et al., 2015; Kuang, 2018; Beucler et al., 2018), but, to the best of our knowledge, not for RCE with localized forcings.

For simulations with added column heating, the prescribed forcing, Q_f, must be distinguished from the total entropy forcing or atmospheric heating rate $\dot{Q}_{atm}$, which includes the atmospheric feedback on the imposed heating. This feedback is composed of changes in the latent, sensible and radiative heat fluxes from the RCE state. Although Q_f represents the main contribution to $\dot{Q}_{atm}$ for simulations with atmospheric heating, surface flux feedbacks contribute up to 40 percent of the entropy forcing in the simulations with heating at the lowest levels (Qlb). For both SSTA and MF, $\dot{Q}_{atm}$ is dominated

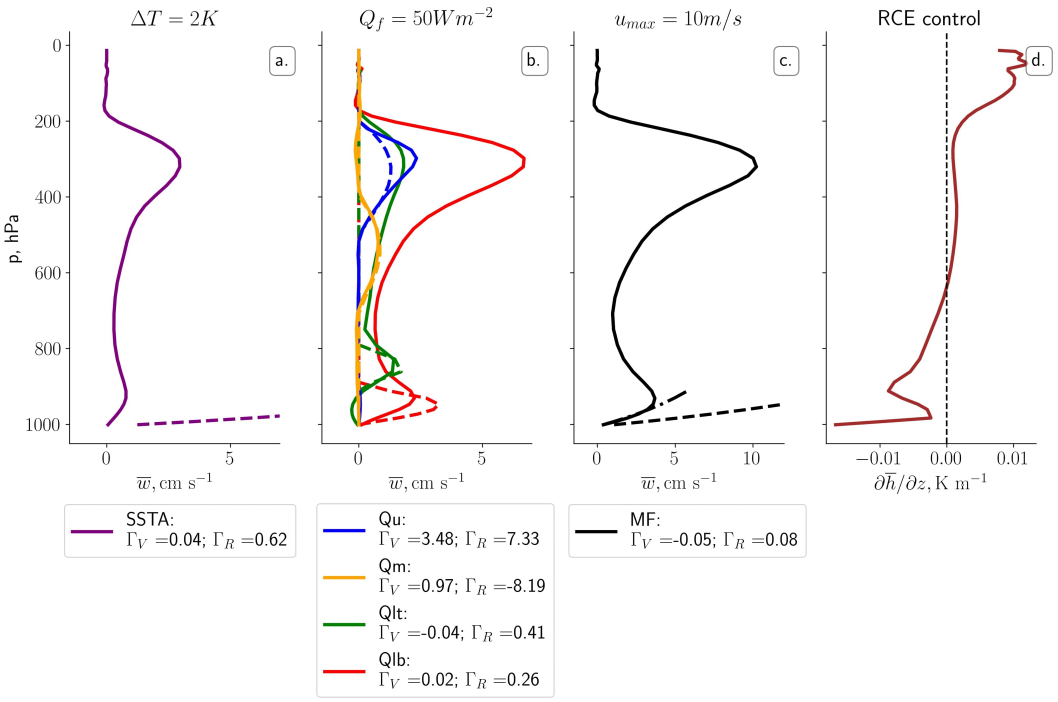

Figure 3. (a-c) Profiles of mean vertical velocity over the reference patch for sea-surface temperature, atmospheric heating, and momentum forcings with the highest magnitudes simulated. Dashed lines represent hypothesized profiles of w based on Bernoulli's principle and mass continuity (for SSTA and MF), and on WTG for atmospheric heating simulations (see text). Dashed-dotted line for MF shows the estimate based on the vertical profile of the forcing and the actual velocity at the patch border. (d) Vertical profile of vertical MSE gradient for the control simulation in RCE. Legend indicates the vertical GMS, Γ_V, and the NGMS, Γ_R (see text).

by changes in the latent heat flux, with sensible heat fluxes accounting for 20 to 30 percent of the total.

The change in precipitation induced by low-level forcings is strongly associated with changes in the column relative humidity (CRH), as indicated in Figure 2b. Consistent with previous observational studies of tropical rainfall (Bretherton et al., 2004; Peters & Neelin, 2006; Rushley et al., 2018; Martinez-Villalobos & Neelin, 2019), precipitation grows approximately exponentially with CRH in our simulations, although the e-folding growth rate found here, 20.8, is higher than values of ~ 15 found by previous work (Bretherton et al., 2004; Rushley et al., 2018). A mechanistic explanation of this well-documented relationship between P and CRH is currently lacking, although our findings suggest that it holds for mechanical as well as thermodynamic forcings.

3.2 Vertical profiles and Gross Moist Stability

The magnitude and structure of the mean vertical velocity profile over the patch, $\overline{w}$, is key to understanding the contrast in precipitation response across different simulations. Low-level forcings, namely SSTA, MF, Qlb and Qlt, show $\overline{w}$ profiles with two peaks: one at lower levels, localized at or close to the location of the forcing, and one in the free troposphere indicating a deep convective response (Figure 3, a. through c.).

In contrast, forcings in the mid- and upper troposphere, Qm and Qu, only produce local responses in $\overline{w}$.

The interaction between the profiles of $\overline{w}$ and moist static energy (MSE) offers a key to understand the precipitation responses in our simulations. The MSE is given by $h = c_pT + gz + L_vq$, where c_p is the specific heat capacity of air at constant pressure, T is the temperature, g is the gravitational acceleration, z is the height, L_v is the latent heat of vaporization of water, and q is the specific humidity. In particular, the vertical gradient of MSE over the domain, $\partial\overline{h}/\partial z$, indicates the locations where energy is imported into or exported out of the atmospheric column. For all low-level forcings, the low-level circulations include ascent at heights where $\frac{\partial\overline{h}}{\partial z} < 0$, which implies a net low-level MSE import and its associated instability. This net import requires in turn an energy export mechanism: this occurs both through the development of the deep circulation, which has a positive GMS and thus helps export energy to the rest of the domain, and through lateral mixing (not quantified).

Are the vertical velocity profiles consistent with our expectations based on required thermodynamic and momentum balances for each forcing? For simulations with localized atmospheric column heating, we can estimate an expected vertical velocity profile through the WTG velocity associated with the forcings, namely

$$w_{WTG} = \frac{\dot{Q}_f}{\overline{ds/dz}}, \tag{9}$$

where $\dot{Q}_f$ is the forcing between the pressure levels specified for each simulation, and $\overline{ds/dz}$ is the vertical gradient of dry static energy averaged over the depth between such pressure levels, and over the extent of the patch. Figure 3b offers a contrast between the mean vertical velocity profile over the patch, and the equivalent w_{WTG} velocities calculated according to equation 9, for simulations with atmospheric column heating at different levels with magnitude of 50 Wm^{-2}. The WTG-inferred vertical velocities capture well the local vertical velocities at the levels where the forcings are prescribed.

For the momentum forcing simulation with $u_{max} = 10\mathrm{m/s}$, we obtain a physically-based null model of the $\overline{w}$ profile for the lowermost 100 hPa by equating the pressure gradient forcing to an equivalent wind convergence through Bernoulli's principle, and integrating the mass continuity equation (see derivation in the Supplement). This approach neglects friction, as well as feedbacks from cold pools over the reference patch, resulting in a large overestimation of the time-mean ascent through the depth of the mixed layer (Figure 3c). However, there is high temporal variability in the ascent over the patch, and the expected profile provides a good upper bound for the strongest circulations at low levels (not shown).

To obtain an analogous null-model for vertical velocity at low levels for SSTA with $\Delta T = 2\mathrm{K}$, we proceed similarly to MF, with the added assumption that the air temperature difference between the patch and the surroundings is constant and equal to ΔT through the depth of the mixed layer (see Supplement). This gives a corresponding pressure difference profile, which, similarly as for MF, yields an expected $\overline{w}$ of approximately 11 cm s^{-1} at 950 hPa, much higher than the simulated mean. This discrepancy is largely due to the boundary-layer temperature anomalies varying between $-0.1\mathrm{K}$ and $0.15\mathrm{K}$ in the lowest kilometer of the atmosphere, a much smaller contrast than the imposed SST anomaly. For both SSTA and MF simulations, these results indicate that stabilizing feedbacks on the near-surface pressure gradients tend to weaken the ascent profile considerably.

We can use the vertical profiles of vertical velocity as well as of dry static energy—given by $s = c_pT + gz$—to estimate the contribution of vertical transport to the NGMS. Following Sobel (2007), Raymond et al. (2009) and Anber et al. (2015), we calculate this vertical GMS, Γ_V, through the expression $\Gamma_V = (1 - M)/M$, where $M = \frac{\langle\overline{w}\partial\overline{h}/\partial z\rangle}{\langle\overline{w}\partial\overline{s}/\partial z\rangle}$,

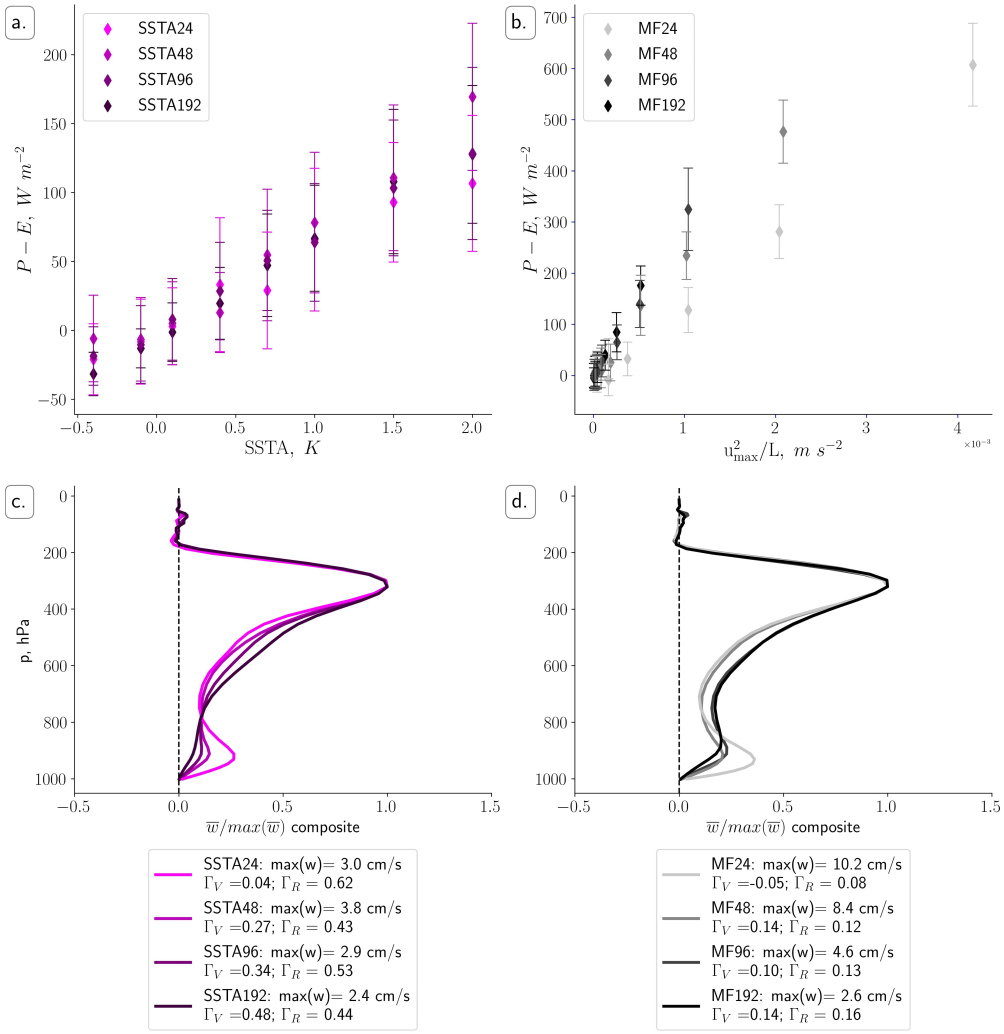

Figure 4. (Top row) Scatter plots of $P - E$ vs. sea-surface temperature anomaly (a.) and the square of the momentum forcing parameter u_{max} divided by patch half-width (b.) for patches of half-widths 24, 48, 96 and 192 km. (Bottom row) Vertical profiles of normalized mean vertical velocities for patches of half-widths of 24, 48, 96 and 192 km for SST anomaly of 2K (c.) and momentum forcing with $u_{max} = 10$m/s (d.). The legend indicates the maximum value of vertical velocity used for normalization, as well as the vertical GMS and the NGMS.

with $\overline{h}$ and $\overline{s}$ the domain-mean MSE and dry static energy values, respectively, and angle brackets denoting the mass-weighted vertical integral from the surface up to the tropopause, taken to be 200 hPa. As indicated in the legend to Figure 3, Γ_V shows poor correspondence with the values of Γ_R for patches of 24 km half-widths. The strength and structure of low-level ascent relative to upper-tropospheric ascent modulates Γ_V, but Γ_V does not correlate strongly with Γ_R for these patch sizes (Figure 3), indicating that horizontal transports are key in determining the exact value of Γ_R for each forcing.

3.3 Patch size effects

We also test the effects of varying the spatial scales on net precipitation by running additional simulations with patches of half-widths 48, 96 and 192 km, for the SSTA

and MF forcings, shown in Figure 4. We note that atmospheric heating simulations tended to aggregate convection for larger patch sizes and strong forcings, and were thus not included.

The behavior of $P-E$ with SST anomaly does not change substantially for different sizes for the range of anomalies considered, although the spread reaches up to 70 Wm^{-2} for the strongest forcing. For the momentum forcing it does exhibit wider spread, since the forcing is applied over the same area while the patch is made larger, leading to a decrease in low-level convergence. The patch size increases cause the theoretical low-level convergence to scale by a factor of 1/L, with L denoting the half-width. However, the curves do not collapse when $P-E$ is plotted against u_{max}/L, indicating other effects are at play.

We have established that the vertical GMS is not a good approximation to the NGMS for a scale of 24 km. However, as the patch is made wider, this discrepancy decreases: for SSTA, the relative error between them drops from close to 100 percent at 24 km, to under 5 percent at 192 km. For MF, it drops from 200 percent at 24 km, to about 6.3 percent at 192 km. This indicates that horizontal transport of MSE becomes negligible at a few hundred kilometers, but plays a major role at small scales.

The values of the NGMS for SSTA do not show a clear trend as the patch is made wider, suggesting that net precipitation does not depend monotonically on the size of the region with anomalous SST. In contrast, a slight but monotonic increase is observed for MF simulations, with the lowest NGMS at the smallest scales. This is consistent with low-level wind convergence driving enhanced rainfall and weakening with increased patch area for fixed u_{max}.

4 Discussion

We have found well-defined values of NGMS for different types of low-level forcing imposed. This suggests that we could in principle provide reasonable estimates for $P-E$ for a given forcing magnitude by interpolating from others. However, the necessity of knowing the NGMS a priori, as well as the substantial variations in NGMS between different types of forcings, severely limit the applicability of the column energetic perspective of Neelin and Held (1987) in predicting precipitation on the basis of environmental forcings. For instance, simulations with mechanically-induced convergence and homogenized surface fluxes show greatly enhanced rainfall over patches with near-zero net atmospheric heating rates.

Our results also show that a prescribed heating in the middle and upper troposphere (above about 700 hPa) does not lead to significant net precipitation enhancement. This is a reminder that knowledge of the total atmospheric column heating rate does not necessarily provide useful information about $P-E$, unless we know how that energy input is distributed in the vertical. The use of a vertically integrated column-energetic budget might overestimate the effectiveness of upper-level heating in driving deep convection, and underestimate the capacity of low-level wind convergence to do the same.

Our simulations provide evidence that the vertical Gross Moist Stability, which only takes into account the profiles of MSE and vertical velocity, is a poor approximation to the NGMS in most of our forcings at scales of 24 km, but improves substantially at scales of a few hundred kilometers. However, the scale at which Γ_V becomes a reasonable approximation of Γ_R is likely to vary depending on the characteristics of low-level convergence. The horizontal component of the GMS, defined effectively in Back and Bretherton (2006) and more explicitly in Raymond et al. (2009), has been shown to play an important role in relatively narrow areas such as the East Pacific ITCZ.

Although studying convective enhancement at large scales without homogenizing radiation would be desirable, it poses the challenge that large domains in RCE produce convective self-aggregation if radiation is made interactive (Muller & Bony, 2015; Wing et al., 2018).

Previous studies have hypothesized that precipitation rates over tropical oceans are governed by the mean moisture saturation deficit of the troposphere, and hence by the CRH (Raymond, 2000; Raymond et al., 2009). Satellite-based observations have since confirmed a close relationship between precipitation and CRH (Bretherton et al., 2004; Peters & Neelin, 2006; Rushley et al., 2018). However, recent theoretical frameworks for tropical moist convection have argued that such relationship can be explained as a consequence of the effect of rainfall on environmental humidity via convective moisture detrainment, or that both precipitation and CRH are affected simultaneously by other causes, such as large-scale ascent and column energetics (Emanuel, 2019; Singh et al., 2019).

Our simulations show that large-scale ascent associated with column energy export, as well as ascent associated with mechanically-induced convergence, can both increase CRH. Hence, the dependence of precipitation on CRH is agnostic to the distinction between mechanical and thermodynamic forcings in our simulations, and is likely not merely due to both variables co-varying with column energetics. This hints at a plausible causal link between them, although more evidence and a mechanistic explanation would be needed to settle the matter.

5 Conclusion

Motivated by the goal of understanding the mechanisms that govern rainfall in the tropics at human-relevant spatial scales, we have explored how different kinds of thermodynamic and mechanical forcings affect precipitation rates in idealized cloud-resolving simulations of a tropical atmospheric domain. Our results indicate that the Normalized Gross Moist Stability, which mediates the relationship between atmospheric heating and net rainfall, is well defined within simulations with low-level forcings, such as localized sea-surface temperature anomalies, low-level atmospheric heating, and mechanically-induced horizontal winds that converge onto a reference area, but varies substantially from one type of forcing to another. Despite their differences in NGMS, our simulations collapse onto the same curve of precipitation versus column relative humidity. This indicates that a mechanistic understanding of the effects of each forcing on $P-E$ might crucially depend on how it affects and maintains column moisture.

6 Open Research

Processed simulation data and scripts are available in the Zenodo repository with DOI:10.5281/zenodo.10086216 (Velez-Pardo, 2023).

References

Anber, U., Wang, S., & Sobel, A. (2015). Effect of surface fluxes versus radiative heating on tropical deep convection. *Journal of the Atmospheric Sciences*, *72*(9), 3378–3388.

Back, L. E., & Bretherton, C. (2006). Geographic variability in the export of moist static energy and vertical motion profiles in the tropical pacific. *Geophysical research letters*, *33*(17).

Beucler, T., Cronin, T., & Emanuel, K. (2018). A linear response framework for radiative-convective instability. *Journal of Advances in Modeling Earth Systems*, *10*(8), 1924–1951.

Bischoff, T., & Schneider, T. (2014). Energetic constraints on the position of the in-

tertropical convergence zone. *Journal of Climate*, *27*(13), 4937–4951.

Boos, W. R., & Korty, R. L. (2016). Regional energy budget control of the intertropical convergence zone and application to mid-holocene rainfall. *Nature Geoscience*, *9*(12), 892–897.

Bretherton, C. S., Peters, M. E., & Back, L. E. (2004). Relationships between water vapor path and precipitation over the tropical oceans. *Journal of climate*, *17*(7), 1517–1528.

Cronin, T. W. (2014). On the choice of average solar zenith angle. *Journal of the Atmospheric Sciences*, *71*(8), 2994–3003.

Cronin, T. W., Emanuel, K. A., & Molnar, P. (2015). Island precipitation enhancement and the diurnal cycle in radiative-convective equilibrium. *Quarterly Journal of the Royal Meteorological Society*, *141*(689), 1017–1034.

Derbyshire, S., Beau, I., Bechtold, P., Grandpeix, J.-Y., Piriou, J.-M., Redelsperger, J.-L., & Soares, P. (2004). Sensitivity of moist convection to environmental humidity. *Quarterly Journal of the Royal Meteorological Society: A journal of the atmospheric sciences, applied meteorology and physical oceanography*, *130*(604), 3055–3079.

Donohoe, A., Marshall, J., Ferreira, D., & Mcgee, D. (2013). The relationship between itcz location and cross-equatorial atmospheric heat transport: From the seasonal cycle to the last glacial maximum. *Journal of Climate*, *26*(11), 3597–3618.

Emanuel, K. (2019). Inferences from simple models of slow, convectively coupled processes. *Journal of the Atmospheric Sciences*, *76*(1), 195–208.

Khairoutdinov, M. F., & Randall, D. A. (2003). Cloud resolving modeling of the arm summer 1997 iop: Model formulation, results, uncertainties, and sensitivities. *Journal of the Atmospheric Sciences*, *60*(4), 607–625.

Kuang, Z. (2012). Weakly forced mock walker cells. *Journal of the Atmospheric Sciences*, *69*(9), 2759–2786.

Kuang, Z. (2018). Linear stability of moist convecting atmospheres. part i: From linear response functions to a simple model and applications to convectively coupled waves. *Journal of the Atmospheric Sciences*, *75*(9), 2889–2907.

Lindzen, R. S., & Nigam, S. (1987). On the role of sea surface temperature gradients in forcing low-level winds and convergence in the tropics. *Journal of Atmospheric Sciences*, *44*(17), 2418–2436.

Marshall, J., Donohoe, A., Ferreira, D., & McGee, D. (2014). The ocean's role in setting the mean position of the inter-tropical convergence zone. *Climate Dynamics*, *42*, 1967–1979.

Martinez-Villalobos, C., & Neelin, J. D. (2019). Why do precipitation intensities tend to follow gamma distributions? *Journal of the Atmospheric Sciences*, *76*(11), 3611–3631.

Muller, C., & Bony, S. (2015). What favors convective aggregation and why? *Geophysical Research Letters*, *42*(13), 5626–5634.

Neelin, J. D., & Held, I. M. (1987). Modeling tropical convergence based on the moist static energy budget. *Monthly Weather Review*, *115*(1), 3–12.

Peters, O., & Neelin, J. D. (2006). Critical phenomena in atmospheric precipitation. *Nature physics*, *2*(6), 393–396.

Raymond, D. J. (2000). Thermodynamic control of tropical rainfall. *Quarterly Journal of the Royal Meteorological Society*, *126*(564), 889–898.

Raymond, D. J., Sessions, S. L., Sobel, A. H., & Fuchs, Ž. (2009). The mechanics of gross moist stability. *Journal of Advances in Modeling Earth Systems*, *1*(3).

Rushley, S. S., Kim, D., Bretherton, C., & Ahn, M.-S. (2018). Reexamining the nonlinear moisture-precipitation relationship over the tropical oceans. *Geophysical research letters*, *45*(2), 1133–1140.

Schneider, T., Bischoff, T., & Haug, G. H. (2014). Migrations and dynamics of the intertropical convergence zone. *Nature*, *513*(7516), 45–53.

Singh, M. S., Warren, R. A., & Jakob, C. (2019). A steady-state model for the relationship between humidity, instability, and precipitation in the tropics. *Journal of Advances in Modeling Earth Systems*, *11*(12), 3973–3994.

Sobel, A. H. (2007). Simple models of ensemble-averaged tropical precipitation and surface wind, given the sea surface temperature. *The global circulation of the atmosphere*, *219*, 251.

Sobel, A. H., & Neelin, J. D. (2006). The boundary layer contribution to intertropical convergence zones in the quasi-equilibrium tropical circulation model framework. *Theoretical and Computational Fluid Dynamics*, *20*, 323–350.

Velez-Pardo, M. (2023). *Accompanying data for "the response of tropical rainfall to idealized small-scale thermal and mechanical forcing", by martin velez-pardo and timothy w. cronin* [dataset]. Zenodo. Retrieved from `https://doi.org/10.5281/zenodo.10086216` doi: 10.5281/zenodo.10086216

Wang, S., & Sobel, A. (2012). Impact of imposed drying on deep convection in a cloud-resolving model. *Journal of Geophysical Research: Atmospheres*, *117*(D2).

Wing, A. A., Emanuel, K., Holloway, C. E., & Muller, C. (2018). Convective self-aggregation in numerical simulations: A review. *Shallow clouds, water vapor, circulation, and climate sensitivity*, 1–25.

Figure 1.

a. SST anomaly

b. Atmospheric heating

c. Low-level momentum forcing

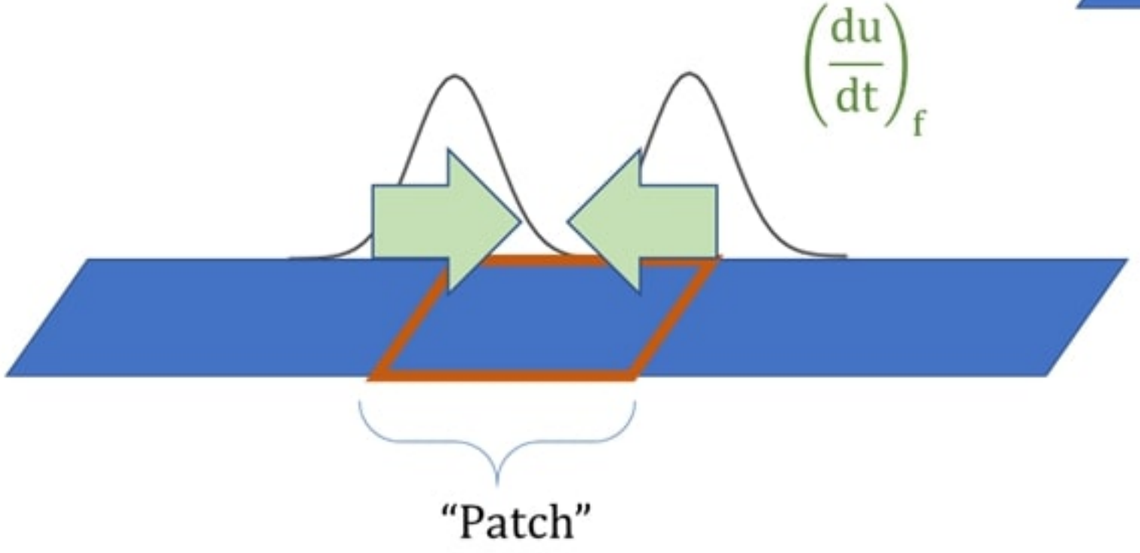

Figure 2.

a.

P-E over patch, Wm^{-2}

$\dot{Q}_{atm}$ over patch, Wm^{-2}

b.

$P/P_0 = \exp(21.2RH)$

P over patch, Wm^{-2}

Column RH

Qu, P-E=(1/7.33)Qatm, R^2=0.15

Qm, P-E=(1/-8.19)Qatm, R^2=0.08

Qlt, P-E=(1/0.41)Qatm, R^2=0.95

Qlb, P-E=(1/0.26)Qatm, R^2=0.99

SSTA, P-E=(1/0.62)Qatm, R^2=0.95

MF, P-E=(1/0.08)Qatm, R^2=0.99

MF(HS)

Figure 3.

$\Delta T = 2K$

$Q_f = 50 W m^{-2}$

$u_{max} = 10 m/s$

RCE control

a.

b.

c.

d.

p, hPa

0

200

400

600

800

1000

0

5

$\overline{w}$, cm s^{-1}

0

5

$\overline{w}$, cm s^{-1}

0

5

10

$\overline{w}$, cm s^{-1}

-0.01

0.00

0.01

$\partial\overline{h}/\partial z$, K m^{-1}

SSTA:
Γ_V =0.04; Γ_R =0.62

Qu:
Γ_V =3.48; Γ_R =7.33

Qm:
Γ_V =0.97; Γ_R =-8.19

Qlt:
Γ_V =-0.04; Γ_R =0.41

Qlb:
Γ_V =0.02; Γ_R =0.26

MF:
Γ_V =-0.05; Γ_R =0.08

Figure 4.

a.

SSTA24
SSTA48
SSTA96
SSTA192

$P-E,\ W\ m^{-2}$

SSTA, K

b.

MF24
MF48
MF96
MF192

$P-E,\ W\ m^{-2}$

$u^2_{max}/L,\ m\ s^{-2}$ $\times 10^{-3}$

c.

p, hPa

$\overline{w}/max(\overline{w})$ composite

SSTA24: max(w)= 3.0 cm/s
Γ_V =0.04; Γ_R = 0.62
SSTA48: max(w)= 3.8 cm/s
Γ_V =0.27; Γ_R = 0.43
SSTA96: max(w)= 2.9 cm/s
Γ_V =0.34; Γ_R = 0.53
SSTA192: max(w)= 2.4 cm/s
Γ_V =0.48; Γ_R = 0.44

d.

$\overline{w}/max(\overline{w})$ composite

MF24: max(w)= 10.2 cm/s
Γ_V =-0.05; Γ_R = 0.08
MF48: max(w)= 8.4 cm/s
Γ_V =0.14; Γ_R = 0.12
MF96: max(w)= 4.6 cm/s
Γ_V =0.10; Γ_R = 0.13
MF192: max(w)= 2.6 cm/s
Γ_V =0.14; Γ_R = 0.16